Author(s): Awan, Hafiz Asad Ali & Tuovinen, Toni & Saarakkala, Seppo E. & Hinkkanen, Marko

Title: Discrete-Time Observer Design for Sensorless Synchronous Motor Drives

Year: 2016

Version: Post print

Please cite the original version:

Awan, Hafiz Asad Ali & Tuovinen, Toni & Saarakkala, Seppo E. & Hinkkanen, Marko. 2016. Discrete-Time Observer Design for Sensorless Synchronous Motor Drives. IEEE Transactions on Industry Applications. 11. ISSN 0093-9994 (printed). DOI: 10.1109/tia.2016.2572105.

Discrete-Time Observer Design for Sensorless Synchronous Motor Drives

Hafiz Asad Ali Awan, Toni Tuovinen, Seppo E. Saarakkala, and Marko Hinkkanen, *Senior Member, IEEE*

***Abstract*—This paper deals with the speed and position estimation of interior permanent-magnet synchronous motor (IPM) and synchronous reluctance motor (SyRM) drives. A speed-adaptive full-order observer is designed and analyzed in the discrete-time domain. The observer design is based on the exact discrete-time motor model, which inherently takes the delays in the control system into account. The proposed observer is experimentally evaluated using a 6.7-kW SyRM drive. The analysis and experimental results indicate that major performance improvements can be obtained with the direct discrete-time design, especially if the sampling frequency is relatively low compared to the fundamental frequency. The ratio below 10 between the sampling and fundamental frequencies is achieved in experiments with the proposed discrete-time design.**

***Index Terms*—Modeling errors, observer, speed sensorless, stability conditions.**

I. Introduction

Synchronous motors with a magnetically anisotropic rotor—such as the interior permanent-magnet synchronous motor (IPM) and the synchronous reluctance motor (SyRM)—are becoming competitors to the induction motor in hybrid and electric vehicles [1], heavy-duty working machines, and industrial applications. In these applications, the maximum speeds and, consequently, the maximum operating frequencies can be very high, while the switching frequency is limited. Hence, the resulting ratio between the switching (sampling) frequency and the maximum fundamental frequency can be even below ten.

Motion-sensorless operation is commonly preferred [2]–[19]. At high speeds, methods based on the back electromotive force (EMF) are favourable. Since the back-EMF-based methods may fail to estimate the rotor position at low speeds and standstill, they could be combined with signal-injection methods [3], [6], [11], [18]. If operation under the load torque at low speeds or position control is required, signal-injection based methods are mandatory. This paper focuses on operation at high fundamental frequencies, and only the back-EMF-based methods will be considered.

Usually, a speed and position observer is first designed in the continuous-time domain and then discretized for a digital processor by means of the forward Euler, symplectic Euler, or Tustin approximations. A drawback of this approach is that the sampling frequency has to be at least 10–20 times higher than the desired maximum fundamental frequency.

Higher fundamental frequencies and improved robustness at a given sampling frequency can be achieved by designing the control system directly in the discrete-time domain [19]–[25]. For the direct discrete-time control design, a hold-equivalent discrete model—including the effects of the zero-order hold (ZOH) and sampler—of the motor drive is needed. The exact closed-form model for surface permanent-magnet synchronous motor (SPM) drives can be found in [20], [21]. For the IPM drives, an approximate discrete model has been proposed in [22], [23] and the exact closed-form model has been recently reported in [25].

A continuous-time gain design [16] for a speed-adaptive full-order observer guarantees the local stability of the estimation-error dynamics at every operating point (except at zero speed) in ideal conditions. However, the effects of the digital implementation were not considered. If the ratio between the sampling frequency and the fundamental frequency is low, the stability conditions derived in [16] are not valid and the system can become unstable.

In this paper, a speed-adaptive full-order observer for sensorless IPM and SyRM drives is designed directly in the discrete-time domain. First, the motor model and the observer design in the continuous-time domain are reviewed in Section II. Then, the main contributions of the paper are presented in Section III:

- A linearized model for the discrete-time estimation-error dynamics is derived.
- A stabilizing observer gain is proposed based on the linearized model. The proposed design decouples the speed-estimation dynamics from the flux-estimation dynamics, which simplifies the tuning procedure.

Section IV describes an example design. In Section V, the proposed discrete-time observer design is evaluated by means of the stability analysis, simulations, and experiments using a 6.7-kW SyRM drive. Furthermore, the discrete-time design is compared to its continuous-time counterpart, which is discretized using the forward Euler approximation.

II. Review: Continuous-Time Model and Observer

Real space vectors will be used. For example, the stator-current vector is $\boldsymbol{i}_\mathrm{s} = [i_\mathrm{d}, i_\mathrm{q}]^\mathrm{T}$, where i_d and i_q are the components of the vector. The identity matrix is $\mathbf{I} = \left[\begin{smallmatrix} 1 & 0 \\ 0 & 1 \end{smallmatrix}\right]$ and the orthogonal rotation matrix is $\mathbf{J} = \left[\begin{smallmatrix} 0 & -1 \\ 1 & 0 \end{smallmatrix}\right]$. Vectors are denoted using boldface lowercase letters and matrices using boldface uppercase letters. Space vectors in stator and

This work was supported in part by ABB Oy and in part by the Academy of Finland.

H. A. A. Awan, S. E. Saarakkala, and M. Hinkkanen are with Aalto University, Department of Electrical Engineering and Automation, 02150 Espoo, Finland (e-mail: hafiz.awan@aalto.fi; seppo.saarakkala@aalto.fi; marko.hinkkanen@aalto.fi).

T. Tuovinen is with ABB Oy Drives, 00380 Helsinki, Finland (e-mail: toni.a.tuovinen@gmail.com).

rotor coordinates are marked with the superscripts s and r, respectively. No superscript is used for space vectors in estimated rotor coordinates.

A. Model

The electrical rotor angle is ϑ_m and the electrical angular rotor speed is $\omega_\mathrm{m} = \mathrm{d}\vartheta_\mathrm{m}/\mathrm{d}t$. The electrical radians are used throughout the paper. In rotor coordinates, the state-space representation corresponding to the standard model of the IPM is

$$\frac{\mathrm{d}\boldsymbol{\psi}_\mathrm{s}^\mathrm{r}(t)}{\mathrm{d}t} = \boldsymbol{A}(t)\boldsymbol{\psi}_\mathrm{s}^\mathrm{r}(t) + \boldsymbol{B}\boldsymbol{u}_\mathrm{s}^\mathrm{r}(t) + \boldsymbol{b}\psi_\mathrm{f} \tag{1a}$$

$$\boldsymbol{i}_\mathrm{s}^\mathrm{r}(t) = \boldsymbol{C}\boldsymbol{\psi}_\mathrm{s}^\mathrm{r}(t) + \boldsymbol{d}\psi_\mathrm{f} \tag{1b}$$

where $\boldsymbol{\psi}_\mathrm{s}$ is the stator flux vector, $\boldsymbol{u}_\mathrm{s}$ is the stator voltage vector, and ψ_f is the permanent-magnet (PM) flux. The system matrices are

$$\boldsymbol{A}(t) = \begin{bmatrix} -R_\mathrm{s}/L_\mathrm{d} & \omega_\mathrm{m}(t) \\ -\omega_\mathrm{m}(t) & -R_\mathrm{s}/L_\mathrm{q} \end{bmatrix}, \quad \boldsymbol{B} = \mathbf{I}, \quad \boldsymbol{b} = \begin{bmatrix} R_\mathrm{s}/L_\mathrm{d} \\ 0 \end{bmatrix}$$
$$\boldsymbol{C} = \begin{bmatrix} 1/L_\mathrm{d} & 0 \\ 0 & 1/L_\mathrm{q} \end{bmatrix}, \quad \boldsymbol{d} = \begin{bmatrix} -1/L_\mathrm{d} \\ 0 \end{bmatrix} \tag{2}$$

where R_s is the stator resistance, L_d is the direct-axis inductance, and L_q is the quadrature-axis inductance. The state-space representation in (1) has two inputs: the stator voltage $\boldsymbol{u}_\mathrm{s}$ and the PM flux ψ_f (which is constant). If $L_\mathrm{d} = L_\mathrm{q}$, the model represents the SPM. If $\psi_\mathrm{f} = 0$, the model of the SyRM is obtained. In the following equations, the time dependency is not explicitly written in order to simplify the notation.

B. Observer Structure

The speed-adaptive full-order observer in estimated rotor coordinates is defined by [9], [16]

$$\frac{\mathrm{d}\hat{\boldsymbol{\psi}}_\mathrm{s}}{\mathrm{d}t} = \hat{\boldsymbol{A}}\hat{\boldsymbol{\psi}}_\mathrm{s} + \boldsymbol{B}\boldsymbol{u}_\mathrm{s} + \boldsymbol{b}\psi_\mathrm{f} + \boldsymbol{K}_\mathrm{c}\tilde{\boldsymbol{i}}_\mathrm{s} \tag{3a}$$

$$\hat{\boldsymbol{i}}_\mathrm{s} = \boldsymbol{C}\hat{\boldsymbol{\psi}}_\mathrm{s} + \boldsymbol{d}\psi_\mathrm{f} \tag{3b}$$

where the estimates are marked by the hat, $\tilde{\boldsymbol{i}}_\mathrm{s} = \hat{\boldsymbol{i}}_\mathrm{s} - \boldsymbol{i}_\mathrm{s}$ is the estimation error of the stator current, and $\boldsymbol{K}_\mathrm{c}$ is the 2×2 gain matrix. Further, the motor parameter estimates are assumed to be accurate in order to simplify the notation. The electrical rotor angle is estimated using

$$\frac{\mathrm{d}\hat{\vartheta}_\mathrm{m}}{\mathrm{d}t} = \hat{\omega}_\mathrm{m}. \tag{4}$$

The proportional-integral (PI) speed-adaptation law is

$$\frac{\mathrm{d}\hat{\omega}_\mathrm{mi}}{\mathrm{d}t} = \boldsymbol{k}_\mathrm{ic}\tilde{\boldsymbol{i}}_\mathrm{s}, \quad \hat{\omega}_\mathrm{m} = \hat{\omega}_\mathrm{mi} + \boldsymbol{k}_\mathrm{pc}\tilde{\boldsymbol{i}}_\mathrm{s} \tag{5}$$

where $\hat{\omega}_\mathrm{mi}$ is the integral state. The gain vectors are $\boldsymbol{k}_\mathrm{ic} = [0, k_\mathrm{ic}]$ and $\boldsymbol{k}_\mathrm{pc} = [0, k_\mathrm{pc}]$, i.e., only the estimation error in the estimated q-axis direction is used for speed estimation. It is worth noticing that the matrix $\hat{\boldsymbol{A}}$ in (3a) depends on the estimated speed $\hat{\omega}_\mathrm{m}$.

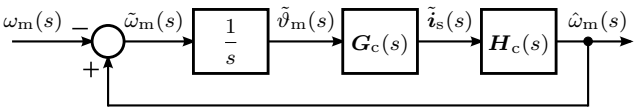

Fig. 1. Linearized estimation-error dynamics for the continuous-time observer design.

C. Estimation-Error Dynamics

1) Nonlinear Dynamics: For analyzing the estimation-error dynamics, the model (1) is first transformed to estimated rotor coordinates as

$$\frac{\mathrm{d}\boldsymbol{\psi}_\mathrm{s}}{\mathrm{d}t} = \boldsymbol{A}'\boldsymbol{\psi}_\mathrm{s} + \boldsymbol{B}\boldsymbol{u}_\mathrm{s} + \boldsymbol{b}'\psi_\mathrm{f} \tag{6a}$$

$$\boldsymbol{i}_\mathrm{s} = \boldsymbol{C}'\boldsymbol{\psi}_\mathrm{s} + \boldsymbol{d}'\psi_\mathrm{f} \tag{6b}$$

where $\boldsymbol{\psi}_\mathrm{s} = \mathrm{e}^{-\tilde{\vartheta}_\mathrm{m}\mathbf{J}}\boldsymbol{\psi}_\mathrm{s}^\mathrm{r}$ and $\tilde{\vartheta}_\mathrm{m} = \hat{\vartheta}_\mathrm{m} - \vartheta_\mathrm{m}$. Other space vectors are transformed similarly. The matrices become

$$\boldsymbol{A}' = \mathrm{e}^{-\tilde{\vartheta}_\mathrm{m}\mathbf{J}}\boldsymbol{A}\mathrm{e}^{\tilde{\vartheta}_\mathrm{m}\mathbf{J}} - \tilde{\omega}_\mathrm{m}\mathbf{J}, \quad \boldsymbol{b}' = \mathrm{e}^{-\tilde{\vartheta}_\mathrm{m}\mathbf{J}}\boldsymbol{b}$$
$$\boldsymbol{C}' = \mathrm{e}^{-\tilde{\vartheta}_\mathrm{m}\mathbf{J}}\boldsymbol{C}\mathrm{e}^{\tilde{\vartheta}_\mathrm{m}\mathbf{J}}, \quad \boldsymbol{d}' = \mathrm{e}^{-\tilde{\vartheta}_\mathrm{m}\mathbf{J}}\boldsymbol{d}. \tag{7}$$

The estimation error of the stator flux is $\tilde{\boldsymbol{\psi}}_\mathrm{s} = \hat{\boldsymbol{\psi}}_\mathrm{s} - \boldsymbol{\psi}_\mathrm{s}$ and the estimation errors of other variables are defined similarly. The nonlinear estimation-error dynamics are

$$\frac{\mathrm{d}\tilde{\boldsymbol{\psi}}_\mathrm{s}}{\mathrm{d}t} = (\hat{\boldsymbol{A}} + \boldsymbol{K}_\mathrm{c}\boldsymbol{C})\tilde{\boldsymbol{\psi}}_\mathrm{s} + (\tilde{\boldsymbol{A}} + \boldsymbol{K}_\mathrm{c}\tilde{\boldsymbol{C}})\boldsymbol{\psi}_\mathrm{s} + (\tilde{\boldsymbol{b}} + \boldsymbol{K}_\mathrm{c}\tilde{\boldsymbol{d}})\psi_\mathrm{f} \tag{8a}$$

$$\tilde{\boldsymbol{i}}_\mathrm{s} = \boldsymbol{C}\tilde{\boldsymbol{\psi}}_\mathrm{s} + \tilde{\boldsymbol{d}}\psi_\mathrm{f} + \tilde{\boldsymbol{C}}\boldsymbol{\psi}_\mathrm{s} \tag{8b}$$

where $\tilde{\boldsymbol{A}} = \hat{\boldsymbol{A}} - \boldsymbol{A}'$, $\tilde{\boldsymbol{b}} = \boldsymbol{b} - \boldsymbol{b}'$, $\tilde{\boldsymbol{C}} = \boldsymbol{C} - \boldsymbol{C}'$, and $\tilde{\boldsymbol{d}} = \boldsymbol{d} - \boldsymbol{d}'$.

2) Linearized Dynamics: The nonlinear dynamics in (8) can be linearized for analysis purposes, leading to [10]

$$\frac{\mathrm{d}\tilde{\boldsymbol{\psi}}_\mathrm{s}}{\mathrm{d}t} = \boldsymbol{A}_{\psi\mathrm{c}}\tilde{\boldsymbol{\psi}}_\mathrm{s} + \boldsymbol{b}_{\vartheta\mathrm{c}}\tilde{\vartheta}_\mathrm{m} \tag{9a}$$

$$\tilde{\boldsymbol{i}}_\mathrm{s} = \boldsymbol{C}\tilde{\boldsymbol{\psi}}_\mathrm{s} + \boldsymbol{d}_{\vartheta\mathrm{c}}\tilde{\vartheta}_\mathrm{m}. \tag{9b}$$

The system matrices are

$$\boldsymbol{A}_{\psi\mathrm{c}} = \boldsymbol{A}_0 + \boldsymbol{K}_\mathrm{c}\boldsymbol{C}, \quad \boldsymbol{b}_{\vartheta\mathrm{c}} = (\boldsymbol{A}_{\psi\mathrm{c}} + \omega_{\mathrm{m}0}\mathbf{J})\boldsymbol{C}^{-1}\boldsymbol{d}_{\vartheta\mathrm{c}}$$
$$\boldsymbol{d}_{\vartheta\mathrm{c}} = (\mathbf{J}\boldsymbol{C} - \boldsymbol{C}\mathbf{J})\,\boldsymbol{\psi}_{\mathrm{s}0} + \mathbf{J}\boldsymbol{d}\psi_\mathrm{f} \tag{10}$$

where the operating-point quantities are marked with the subscript 0. The system (9) can be represented by the transfer-function matrix

$$\boldsymbol{G}_\mathrm{c}(s) = \boldsymbol{C}(s\mathbf{I} - \boldsymbol{A}_{\psi\mathrm{c}})^{-1}\boldsymbol{b}_{\vartheta\mathrm{c}} + \boldsymbol{d}_{\vartheta\mathrm{c}} \tag{11}$$

from $\tilde{\vartheta}_\mathrm{m}(s)$ to $\tilde{\boldsymbol{i}}_\mathrm{s}(s)$. Further, the speed-adaptation law (5) corresponds to the transfer-function matrix $\boldsymbol{H}_\mathrm{c}(s) = \boldsymbol{k}_\mathrm{pc} + \boldsymbol{k}_\mathrm{ic}/s$ from $\tilde{\boldsymbol{i}}_\mathrm{s}(s)$ to $\hat{\omega}_\mathrm{m}(s)$. Fig. 1 shows the block diagram of the linearized estimation-error dynamics. The closed-loop transfer function from the actual speed to the estimated speed is

$$\frac{\hat{\omega}_\mathrm{m}(s)}{\omega_\mathrm{m}(s)} = \frac{\boldsymbol{H}_\mathrm{c}(s)\boldsymbol{G}_\mathrm{c}(s)}{s + \boldsymbol{H}_\mathrm{c}(s)\boldsymbol{G}_\mathrm{c}(s)}. \tag{12}$$

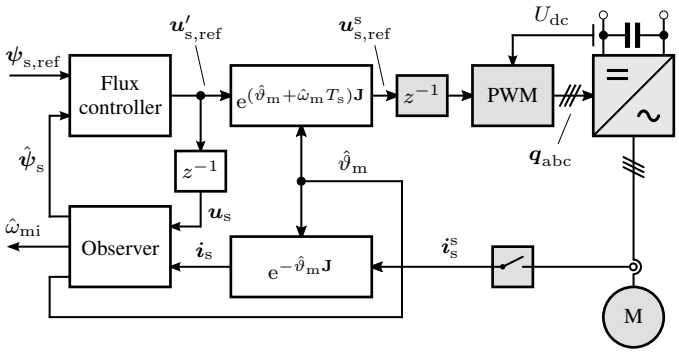

Fig. 2. Sensorless control system. The discrete-time plant model includes the gray blocks: motor, PWM, and computational time delay z^{-1}. The white blocks represent the discrete-time control algorithm. For discrete-time modeling, the PWM is replaced with the ZOH and the gate signals $\boldsymbol{q}_{\mathrm{abc}}$ are replaced with the duty ratios $\boldsymbol{d}_{\mathrm{abc}}$.

D. Gain Selection

First, to simplify the notation in the following, an auxiliary variable

$$\beta = (L_{\mathrm{d}} - L_{\mathrm{q}})\frac{i_{\mathrm{q}}}{\psi'_{\mathrm{f}}} \tag{13}$$

is defined, where the denominator $\psi'_{\mathrm{f}} = \psi_{\mathrm{f}} + (L_{\mathrm{d}} - L_{\mathrm{q}})i_{\mathrm{d}}$ can be interpreted as a fictitious flux [5], [15]. As special cases, $\beta = 0$ holds for SPMs and $\beta = i_{\mathrm{q}}/i_{\mathrm{d}}$ for SyRMs.

The fourth-order system shown in Fig. 1 is complicated and the gains can be difficult to tune. In order to simplify the tuning procedure, the speed-estimation dynamics and the flux-estimation dynamics can be decoupled by zeroing $\boldsymbol{b}_{\vartheta\mathrm{c}}$, leading to $\boldsymbol{G}_{\mathrm{c}}(s) = \boldsymbol{d}_{\vartheta\mathrm{c}}$. From (10), the observer gain yielding $\boldsymbol{b}_{\vartheta\mathrm{c}} = \boldsymbol{0}$ can be solved as [16]

$$\boldsymbol{K}_{\mathrm{c}} = \begin{bmatrix} R_{\mathrm{s}} + L_{\mathrm{d}}k_{1\mathrm{c}} & -\beta L_{\mathrm{q}}k_{1\mathrm{c}} \\ L_{\mathrm{d}}k_{2\mathrm{c}} & R_{\mathrm{s}} - \beta L_{\mathrm{q}}k_{2\mathrm{c}} \end{bmatrix} \tag{14}$$

where

$$k_{1\mathrm{c}} = -\frac{b_{\mathrm{c}} + \beta(c_{\mathrm{c}}/\hat{\omega}_{\mathrm{m}} - \hat{\omega}_{\mathrm{m}})}{\beta^2 + 1}, \quad k_{2\mathrm{c}} = \frac{\beta b_{\mathrm{c}} - c_{\mathrm{c}}/\hat{\omega}_{\mathrm{m}} + \hat{\omega}_{\mathrm{m}}}{\beta^2 + 1}. \tag{15}$$

The speed-adaptation gains are $k_{\mathrm{pc}} = L_{\mathrm{q}}d_{\mathrm{c}}/\psi'_{\mathrm{f}}$ and $k_{\mathrm{ic}} = L_{\mathrm{q}}e_{\mathrm{c}}/\psi'_{\mathrm{f}}$. With this gain selection, the characteristic polynomial of the estimation-error dynamics becomes $(s^2 + b_{\mathrm{c}}s + c_{\mathrm{c}})(s^2 + d_{\mathrm{c}}s + e_{\mathrm{c}})$, where the design parameters are $b_{\mathrm{c}} > 0$, $c_{\mathrm{c}} > 0$, $d_{\mathrm{c}} > 0$, and $e_{\mathrm{c}} > 0$, which may depend on the operating point.

The design parameters b_{c} and c_{c} determine the flux-estimation error dynamics. In order to keep the observer gains (15) within reasonable limits, the design parameters should be selected in such a way that the closed-loop poles of the flux estimator remain in the vicinity of the open-loop system poles, i.e., the eigenvalues of the system matrix $\boldsymbol{A}(t)$ in (1).

The design parameters d_{c} and e_{c} determine the speed-adaptation dynamics. The resulting closed-loop transfer function from the actual speed to the estimated speed is

$$\frac{\hat{\omega}_{\mathrm{m}}(s)}{\omega_{\mathrm{m}}(s)} = \frac{d_{\mathrm{c}}s + e_{\mathrm{c}}}{s^2 + d_{\mathrm{c}}s + e_{\mathrm{c}}}. \tag{16}$$

With accurate model parameters, the estimation-error dynamics are locally stable in every operating point (marginally stable at zero speed). This observer design is a subset of all possible stable designs. However, it is easier to tune two second-order systems than one fourth-order system, which is a clear advantage of this gain selection.

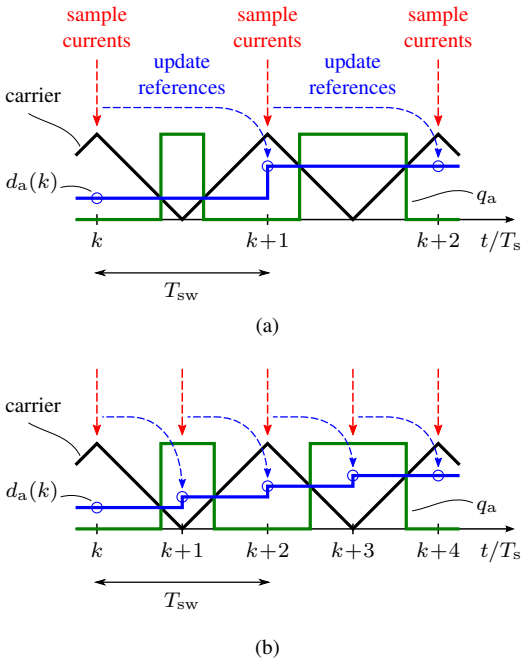

Fig. 3. PWM update and sampling schemes: (a) single-update PWM with sampling at the start of the switching period T_{sw}; (b) double-update PWM with sampling twice per the switching period. The triangular carrier signal, a-phase duty ratio $d_{\mathrm{a}}(k)$, and resulting a-phase gate signal q_{a} are illustrated. The duty ratios $d_{\mathrm{b}}(k)$ and $d_{\mathrm{c}}(k)$ (not shown) of the other two phases are updated simultaneously with $d_{\mathrm{a}}(k)$ and compared to the same carrier signal.

III. Discrete-Time Model and Observer

Fig. 2 shows a sensorless control system, which is the framework for the discrete-time observer. In this paper, the flux-linkage controller is used, but the proposed observer could also be used together with the current controller. It was found out that controlling the fluxes instead of the currents makes the system more robust against noise, originating mainly from spatial harmonics and nonlinear saturation characteritics of the motor. Similar observations have been made in [26]. In the following, the pulse-width modulator (PWM) update and sampling scheme is briefly introduced. Then, the discrete-time model and the observer design are presented.

A. PWM Update and Sampling

Sampling of the stator currents is synchronized with the PWM. Fig. 3 illustrates two common PWM update and sampling schemes [27], [28], which both are directly compatible with the proposed discrete-time design.[1] The sampling period is denoted by T_{s} and the discrete-time index by k. At every time step, the duty ratios $\boldsymbol{d}_{\mathrm{abc}} = [d_{\mathrm{a}}, d_{\mathrm{b}}, d_{\mathrm{c}}]^{\mathrm{T}}$ for each phase

[1]The single-update PWM with sampling in the middle of the switching period is the third commonly used PWM update and sampling scheme. Some modifications in the discrete-time model would be needed for this sampling scheme.

are calculated from the stator voltage reference $\boldsymbol{u}^{\mathrm{s}}_{\mathrm{s,ref}}$ by means of the space-vector PWM algorithm. The gate signals $\boldsymbol{q}_{\mathrm{abc}} = [q_{\mathrm{a}}, q_{\mathrm{b}}, q_{\mathrm{c}}]^{\mathrm{T}}$ are obtained by comparing the duty ratios $\boldsymbol{d}_{\mathrm{abc}}$ with the carrier signal.

As illustrated in Fig. 3, the PWM update has one-sampling-period time delay due to the finite computation time. The gray block z^{-1} in Fig. 2 models this computational delay. The effect of the time delay on the voltage angle is compensated for in the coordinate transformation of the reference voltage.

In the following discrete-time model, the average of the stator voltage over the sampling period T_{s} is considered, i.e.,

$$\boldsymbol{u}^{\mathrm{s}}_{\mathrm{s}}(k) = \frac{2U_{\mathrm{dc}}}{3}\begin{bmatrix}1 & -\frac{1}{2} & -\frac{1}{2}\\ 0 & \frac{\sqrt{3}}{2} & -\frac{\sqrt{3}}{2}\end{bmatrix}\boldsymbol{d}_{\mathrm{abc}}(k) \tag{17}$$

where U_{dc} is the DC-link voltage. The stator voltage in stator coordinates is assumed to be piecewise constant between two consecutive sampling instants, which corresponds to the ZOH in stator coordinates. In other words, the stator voltage $\boldsymbol{u}^{\mathrm{s}}_{\mathrm{s}}(t)$ is constant during $kT_{\mathrm{s}} < t < (k+1)T_{\mathrm{s}}$.

B. Exact Discrete Hold-Equivalent Model

The exact discrete-time state-space representation of (1) in rotor coordinates is given by

$$\boldsymbol{\psi}^{\mathrm{r}}_{\mathrm{s}}(k+1) = \boldsymbol{\Phi}\boldsymbol{\psi}^{\mathrm{r}}_{\mathrm{s}}(k) + \boldsymbol{\Gamma}\boldsymbol{u}^{\mathrm{r}}_{\mathrm{s}}(k) + \boldsymbol{\gamma}\psi_{\mathrm{f}} \tag{18a}$$
$$\boldsymbol{i}^{\mathrm{r}}_{\mathrm{s}}(k) = \boldsymbol{C}\boldsymbol{\psi}^{\mathrm{r}}_{\mathrm{s}}(k) + \boldsymbol{d}\psi_{\mathrm{f}} \tag{18b}$$

where the system matrices are [25]

$$\begin{aligned}\boldsymbol{\Phi} &= \mathrm{e}^{\boldsymbol{A}T_{\mathrm{s}}} = \begin{bmatrix}\phi_{11} & -\phi_{21}\\ \phi_{21} & \phi_{22}\end{bmatrix}, \quad \boldsymbol{\gamma} = \int_0^{T_{\mathrm{s}}} \mathrm{e}^{\boldsymbol{A}\tau}\mathrm{d}\tau\cdot\boldsymbol{b} = \begin{bmatrix}\gamma_1\\ \gamma_2\end{bmatrix}\\ \boldsymbol{\Gamma} &= \int_0^{T_{\mathrm{s}}} \mathrm{e}^{\boldsymbol{A}\tau}\mathrm{e}^{\omega_{\mathrm{m}}\tau\mathbf{J}}\mathrm{d}\tau\cdot\mathrm{e}^{-\omega_{\mathrm{m}}T_{\mathrm{s}}\mathbf{J}} = \begin{bmatrix}\gamma_{11} & \gamma_{12}\\ \gamma_{21} & \gamma_{22}\end{bmatrix}.\end{aligned} \tag{19}$$

In the above equation for $\boldsymbol{\Gamma}$, the ZOH of the stator voltage is modeled in stationary coordinates, where it physically is. Hence, the model inherently takes the ZOH delay properly into account. The closed-form expressions of the matrix elements are given in Appendix A. If the exact expressions are computationally too demanding, approximate expressions (series expansions) could be used instead.

C. Observer Structure

The discrete-time observer in estimated rotor coordinates is defined by

$$\hat{\boldsymbol{\psi}}_{\mathrm{s}}(k+1) = \hat{\boldsymbol{\Phi}}\hat{\boldsymbol{\psi}}_{\mathrm{s}}(k) + \hat{\boldsymbol{\Gamma}}\boldsymbol{u}_{\mathrm{s}}(k) + \hat{\boldsymbol{\gamma}}\psi_{\mathrm{f}} + \boldsymbol{K}\tilde{\boldsymbol{i}}_{\mathrm{s}}(k) \tag{20a}$$
$$\hat{\boldsymbol{i}}_{\mathrm{s}}(k) = \boldsymbol{C}\hat{\boldsymbol{\psi}}_{\mathrm{s}}(k) + \boldsymbol{d}\psi_{\mathrm{f}} \tag{20b}$$

where $\boldsymbol{K}$ is the gain matrix. It is worth noticing that the matrices $\hat{\boldsymbol{\Phi}}$, $\hat{\boldsymbol{\Gamma}}$, and $\hat{\boldsymbol{\gamma}}$ in the discrete-time observer are functions of the estimated speed $\hat{\omega}_{\mathrm{m}}$. This differs from the continuous-time case, where only the system matrix $\hat{\boldsymbol{A}}$ depends on the estimated speed. As shown in Fig. 2, the effect of the computational delay on the stator voltage is compensated for by intentionally delaying the voltage input of the observer, i.e., $\boldsymbol{u}_{\mathrm{s}}(k) = \boldsymbol{u}_{\mathrm{s,ref}}(k-1)$. As mentioned before, the effect of the ZOH is inherently included in the exact discrete-time plant model. A discrete-time rotor-position estimator is

$$\hat{\vartheta}_{\mathrm{m}}(k+1) = \hat{\vartheta}_{\mathrm{m}}(k) + T_{\mathrm{s}}\hat{\omega}_{\mathrm{m}}(k) \tag{21}$$

and the speed-adaptation law is

$$\hat{\omega}_{\mathrm{mi}}(k+1) = \hat{\omega}_{\mathrm{mi}}(k) + T_{\mathrm{s}}\boldsymbol{k}_{\mathrm{i}}\tilde{\boldsymbol{i}}_{\mathrm{s}}(k) \tag{22a}$$
$$\hat{\omega}_{\mathrm{m}}(k) = \hat{\omega}_{\mathrm{mi}}(k) + \boldsymbol{k}_{\mathrm{p}}\tilde{\boldsymbol{i}}_{\mathrm{s}}(k) \tag{22b}$$

where $\boldsymbol{k}_{\mathrm{p}} = [0, k_{\mathrm{p}}]$ and $\boldsymbol{k}_{\mathrm{i}} = [0, k_{\mathrm{i}}]$ are the gain vectors. The integral state $\hat{\omega}_{\mathrm{mi}}$ can be used as an input signal in outer control loops (e.g., in the speed controller), while the observer state matrices in (20) and the rotor position estimation in (21) depend on $\hat{\omega}_{\mathrm{m}}$.

D. Estimation-Error Dynamics

1) Nonlinear Dynamics: For analyzing the estimation-error dynamics, the model (18) is transformed to estimated rotor coordinates as

$$\boldsymbol{\psi}_{\mathrm{s}}(k+1) = \boldsymbol{\Phi}'\boldsymbol{\psi}_{\mathrm{s}}(k) + \boldsymbol{\Gamma}'\boldsymbol{u}_{\mathrm{s}}(k) + \boldsymbol{\gamma}'\psi_{\mathrm{f}} \tag{23a}$$
$$\boldsymbol{i}_{\mathrm{s}}(k) = \boldsymbol{C}'\boldsymbol{\psi}_{\mathrm{s}}(k) + \boldsymbol{d}'\psi_{\mathrm{f}} \tag{23b}$$

where

$$\begin{aligned}\boldsymbol{\Phi}' &= \mathrm{e}^{-\tilde{\vartheta}_{\mathrm{m}}(k+1)\mathbf{J}}\boldsymbol{\Phi}\mathrm{e}^{\tilde{\vartheta}_{\mathrm{m}}(k)\mathbf{J}}\\ \boldsymbol{\Gamma}' &= \mathrm{e}^{-\tilde{\vartheta}_{\mathrm{m}}(k+1)\mathbf{J}}\boldsymbol{\Gamma}\mathrm{e}^{\tilde{\vartheta}_{\mathrm{m}}(k)\mathbf{J}}, \quad \boldsymbol{\gamma}' = \mathrm{e}^{-\tilde{\vartheta}_{\mathrm{m}}(k+1)\mathbf{J}}\boldsymbol{\gamma}\\ \boldsymbol{C}' &= \mathrm{e}^{-\tilde{\vartheta}_{\mathrm{m}}(k)\mathbf{J}}\boldsymbol{C}\mathrm{e}^{\tilde{\vartheta}_{\mathrm{m}}(k)\mathbf{J}}, \quad \boldsymbol{d}' = \mathrm{e}^{-\tilde{\vartheta}_{\mathrm{m}}(k)\mathbf{J}}\boldsymbol{d}.\end{aligned} \tag{24}$$

The nonlinear estimation-error dynamics become

$$\begin{aligned}\tilde{\boldsymbol{\psi}}_{\mathrm{s}}(k+1) &= (\hat{\boldsymbol{\Phi}} + \boldsymbol{K}\boldsymbol{C})\tilde{\boldsymbol{\psi}}_{\mathrm{s}}(k) + (\tilde{\boldsymbol{\Phi}} + \boldsymbol{K}\tilde{\boldsymbol{C}})\boldsymbol{\psi}_{\mathrm{s}}(k)\\ &\quad + (\tilde{\boldsymbol{\gamma}} + \boldsymbol{K}\tilde{\boldsymbol{d}})\psi_{\mathrm{f}} + \tilde{\boldsymbol{\Gamma}}\boldsymbol{u}_{\mathrm{s}}(k)\end{aligned} \tag{25a}$$
$$\tilde{\boldsymbol{i}}_{\mathrm{s}}(k) = \boldsymbol{C}\tilde{\boldsymbol{\psi}}_{\mathrm{s}}(k) + \tilde{\boldsymbol{d}}\psi_{\mathrm{f}} + \tilde{\boldsymbol{C}}\boldsymbol{\psi}_{\mathrm{s}}(k) \tag{25b}$$

where $\tilde{\boldsymbol{\Phi}} = \hat{\boldsymbol{\Phi}} - \boldsymbol{\Phi}'$ and other matrices are defined similarly.

2) Linearized Dynamics: Linearization of (25) leads to

$$\tilde{\boldsymbol{\psi}}_{\mathrm{s}}(k+1) = \boldsymbol{A}_{\psi}\tilde{\boldsymbol{\psi}}_{\mathrm{s}}(k) + \boldsymbol{b}_{\vartheta}\tilde{\vartheta}_{\mathrm{m}}(k) + \boldsymbol{b}_{\omega}\tilde{\omega}_{\mathrm{m}}(k) \tag{26a}$$
$$\tilde{\boldsymbol{i}}_{\mathrm{s}}(k) = \boldsymbol{C}\tilde{\boldsymbol{\psi}}_{\mathrm{s}}(k) + \boldsymbol{d}_{\vartheta}\tilde{\vartheta}_{\mathrm{m}}(k) \tag{26b}$$

where the system matrices are

$$\begin{aligned}\boldsymbol{A}_{\psi} &= \boldsymbol{\Phi}_0 + \boldsymbol{K}\boldsymbol{C}, \quad \boldsymbol{d}_{\vartheta} = (\mathbf{J}\boldsymbol{C} - \boldsymbol{C}\mathbf{J})\,\boldsymbol{\psi}_{\mathrm{s}0} + \mathbf{J}\boldsymbol{d}\psi_{\mathrm{f}}\\ \boldsymbol{b}_{\omega} &= \left(\left.\frac{\partial\boldsymbol{\Phi}}{\partial\omega_{\mathrm{m}}}\right|_0 + T_{\mathrm{s}}\mathbf{J}\boldsymbol{\Phi}_0\right)\boldsymbol{\psi}_{\mathrm{s}0} + \left(\left.\frac{\partial\boldsymbol{\gamma}}{\partial\omega_{\mathrm{m}}}\right|_0 + T_{\mathrm{s}}\mathbf{J}\boldsymbol{\gamma}_0\right)\psi_{\mathrm{f}}\\ &\quad + \left(\left.\frac{\partial\boldsymbol{\Gamma}}{\partial\omega_{\mathrm{m}}}\right|_0 + T_{\mathrm{s}}\mathbf{J}\boldsymbol{\Gamma}_0\right)\boldsymbol{u}_{\mathrm{s}0}\\ \boldsymbol{b}_{\vartheta} &= (\mathbf{J}\boldsymbol{\Phi}_0 - \boldsymbol{\Phi}_0\mathbf{J})\boldsymbol{\psi}_{\mathrm{s}0} + \mathbf{J}\boldsymbol{\gamma}_0\psi_{\mathrm{f}} + \boldsymbol{K}\boldsymbol{d}_{\vartheta}\\ &\quad + (\mathbf{J}\boldsymbol{\Gamma}_0 - \boldsymbol{\Gamma}_0\mathbf{J})\,\boldsymbol{u}_{\mathrm{s}0}.\end{aligned} \tag{27}$$

The elements of $\boldsymbol{b}_{\omega}$ approach zero as the sampling period T_{s} approaches zero. The transfer-function matrix from $\tilde{\vartheta}_{\mathrm{m}}(z)$ to $\tilde{\boldsymbol{i}}_{\mathrm{s}}(z)$ is

$$\boldsymbol{G}(z) = \boldsymbol{C}(z\mathbf{I} - \boldsymbol{A}_{\psi})^{-1}\boldsymbol{b}_{\vartheta} + \boldsymbol{d}_{\vartheta} \tag{28}$$

and the transfer-function matrix from $\tilde{\omega}_{\mathrm{m}}(z)$ to $\tilde{\boldsymbol{i}}_{\mathrm{s}}(z)$ is

$$\boldsymbol{G}_{\omega}(z) = \boldsymbol{C}(z\mathbf{I} - \boldsymbol{A}_{\psi})^{-1}\boldsymbol{b}_{\omega}. \tag{29}$$

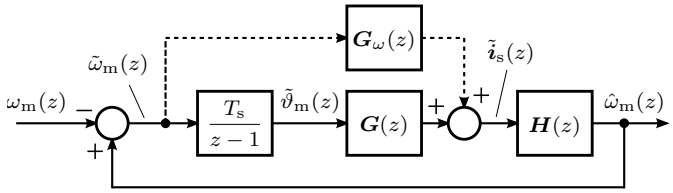

Fig. 4. Linearized estimation-error dynamics for the discrete-time observer design. The dashed line disappears if $\boldsymbol{b}_\omega = \boldsymbol{0}$ is assumed.

The transfer-function matrix from $\tilde{\boldsymbol{i}}_\mathrm{s}(z)$ to $\hat{\omega}_\mathrm{m}(z)$, corresponding to the adaptation law (22), is $\boldsymbol{H}(z) = \boldsymbol{k}_\mathrm{p} + T_\mathrm{s}\boldsymbol{k}_\mathrm{i}/(z-1)$. Fig. 4 presents the block diagram of the linearized estimation-error dynamics.

E. Gain Selection

The linearized system in Fig. 4 is of the fourth order, and in general, explicit expressions for the gain selection may not exist. In order to obtain an approximate solution, $\boldsymbol{b}_\omega = \boldsymbol{0}$ is assumed. It is also worth noticing that $\boldsymbol{b}_\omega$ does not depend on the observer gain, i.e., it cannot be affected by the gain selection. On the other hand, $\boldsymbol{b}_\vartheta = \boldsymbol{0}$ can be forced, if the observer gain

$$\boldsymbol{K} = \begin{bmatrix} L_\mathrm{d}k_1 & L_\mathrm{q}(v-\beta k_1) \\ L_\mathrm{d}k_2 & L_\mathrm{q}(w-\beta k_2) \end{bmatrix} \tag{30}$$

with

$$\begin{aligned} v = {} & \big[u_\mathrm{q}(\gamma_{11}-\gamma_{22}) - u_\mathrm{d}(\gamma_{12}+\gamma_{21}) \\ & + (\phi_{11}-\phi_{22})\hat{\psi}_\mathrm{q} - \gamma_2\psi_\mathrm{f}\big]/\psi'_\mathrm{f} \end{aligned} \tag{31a}$$

$$\begin{aligned} w = {} & \big[u_\mathrm{d}(\gamma_{11}-\gamma_{22}) + u_\mathrm{q}(\gamma_{12}+\gamma_{21}) \\ & + (\phi_{11}-\phi_{22})\hat{\psi}_\mathrm{d} + \gamma_1\psi_\mathrm{f}\big]/\psi'_\mathrm{f} \end{aligned} \tag{31b}$$

is selected. This design principle is analogous to the continuous-time case presented in Section II-D.

The fourth-order characteristic polynomial is expressed as a product of two second-order polynomials $(z^2+bz+c)(z^2+dz+e)$, where the first part corresponds to the flux estimation and the second part corresponds to the speed adaptation. The resulting stabilizing gain selection is

$$\begin{aligned} k_1 = {} & -\big[(\phi_{11}^2 + b\phi_{11} - \phi_{21}^2 + \phi_{21}v + c)\beta \\ & + (\phi_{11}+\phi_{22}+b+w)(v-\phi_{21})\big]/D \end{aligned} \tag{32a}$$

$$\begin{aligned} k_2 = {} & \big[\phi_{21}^2 - \phi_{21}v - c - (\phi_{22}+w)(\phi_{22}+b+w) \\ & - (\phi_{11}+\phi_{22}+b+w)\phi_{21}\beta\big]/D \end{aligned} \tag{32b}$$

where $D = v - \phi_{21}(1+\beta^2) + (\phi_{11}-\phi_{22}-w)\beta$. It is to be noted that as the speed and torque approach zero, the gains k_1 and k_2 approach the following values:

$$k_1 = \frac{\phi_{11}^2 + b\phi_{11} + c}{\phi_{22} - \phi_{11} + w}, \quad k_2 = 0. \tag{33}$$

The speed-adaptation gains are

$$k_\mathrm{p} = \frac{L_\mathrm{q}(d+2)}{T_\mathrm{s}\psi'_\mathrm{f}}, \quad k_\mathrm{i} = \frac{L_\mathrm{q}(d+e+1)}{T_\mathrm{s}^2\psi'_\mathrm{f}}. \tag{34}$$

In order to guarantee stable operation, the discrete-time design parameters b, c, d, and e have to be selected so that the roots of the corresponding polynomials, z^2+bz+c and z^2+dz+e, remain inside the unit circle in every operating point. This condition is fulfilled, when the continuous-time parameters b_c and c_c are mapped to their discrete-time equivalents as

$$b = -2\mathrm{e}^{-b_\mathrm{c}T_\mathrm{s}/2}\cosh\left(T_\mathrm{s}\sqrt{b_\mathrm{c}^2/4 - c_\mathrm{c}}\right), \quad c = \mathrm{e}^{-b_\mathrm{c}T_\mathrm{s}}. \tag{35}$$

The parameters d and e are obtained from d_c and e_c in a similar manner. Assuming $\boldsymbol{b}_\omega = 0$ and accurate model parameters, this gain selection yields locally stable position estimation in every operating point except zero speed (where the system is only marginally stable). Due to the assumption $\boldsymbol{b}_\omega = 0$, the actual poles of the linearized closed-loop system are slightly misplaced from the desired values even with exact parameter estimates.

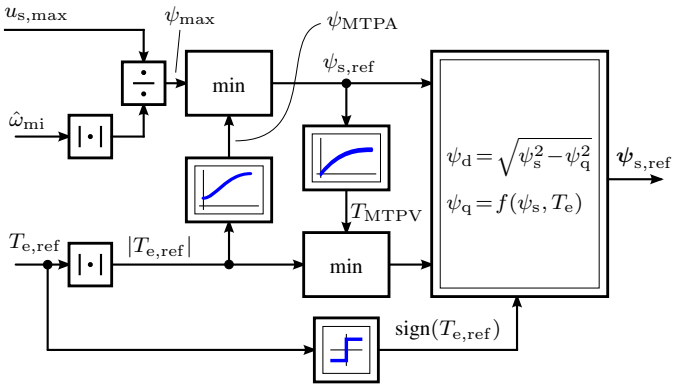

Fig. 5. Calculation of the flux reference. The torque reference $T_\mathrm{e,ref}$ comes from the speed controller, whose feedback signal is the speed estimate $\hat{\omega}_\mathrm{mi}$. The maximum available voltage $u_\mathrm{s,max}$ depends on the measured DC-link voltage. The stator flux corresponding to the MTPA condition is denoted by ψ_MTPA and the torque limit corresponding to the MTPV condition by T_MTPV.

IV. Experimental Setup and Parameters

A 6.7-kW four-pole SyRM drive is considered. The rated values are: speed 3175 r/min; frequency 105.8 Hz; line-to-line rms voltage 370 V; rms current 15.5 A; and torque 20.1 Nm. A servo motor was used as a loading machine. The total moment of inertia is 0.015 kgm^2 (2.7 times the inertia of the SyRM rotor). The actual rotor speed ω_m and position ϑ_m are measured using an incremental encoder for monitoring purposes.

The sensorless control method was implemented in an OPAL-RT OP5600 rapid prototyping system. It is equipped with a Xilinx Virtex-6 FPGA, which is used for the single-update PWM and sampling scheme shown in Fig. 3(a), i.e., the switching frequency equals the sampling frequency. The stator currents and the DC-link voltage are measured for feedback according to Fig. 2. A simple current feedforward compensation for dead times and power device voltage drops is applied. In the observer and control system, the magnetic saturation of the SyRM is modeled according to [29].

The flux controller and its tuning is based on the discrete-time controller presented in [25]. Compared to [25], only the state variable to be controlled has been changed from the

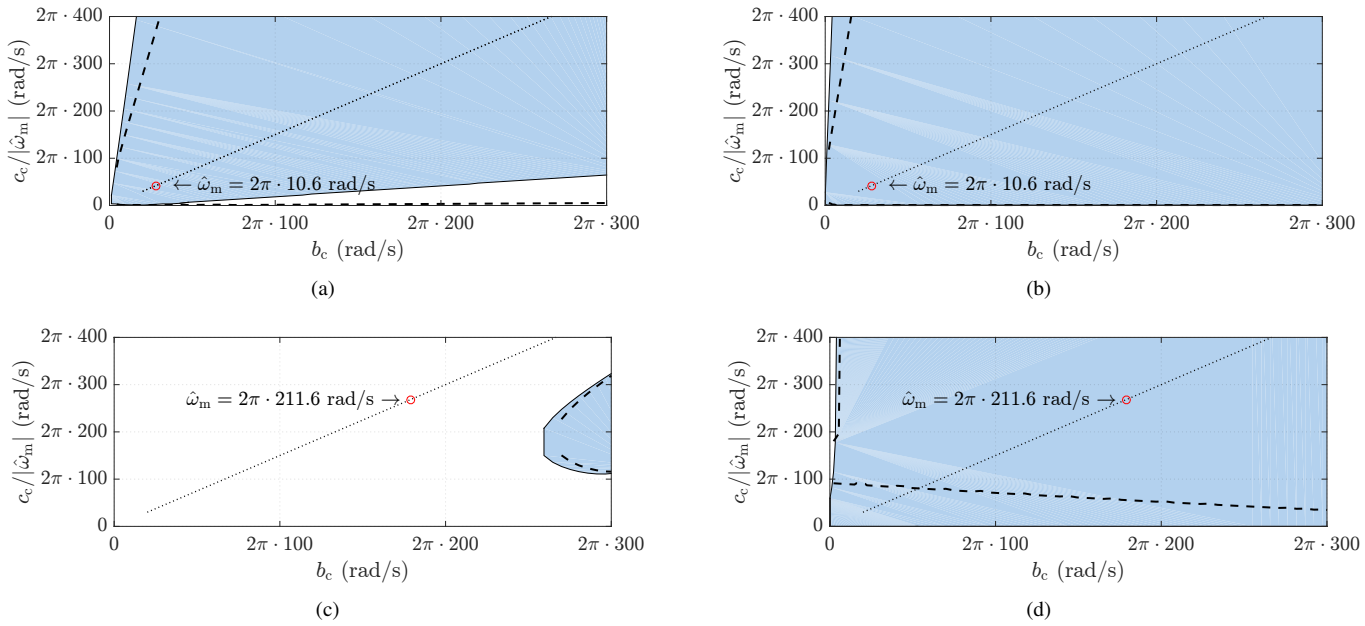

Fig. 6. Stability regions in the design parameter space: (a) continuous-time design at the operating point $\omega_m = 0.1$ p.u., $i_d = 0.55$ p.u., and $i_q = 0.90$ p.u.; (b) direct discrete-time design at $\omega_m = 0.1$ p.u., $i_d = 0.55$ p.u., and $i_q = 0.90$ p.u.; (c) continuous-time design at $\omega_m = 2$ p.u. and $i_d = i_q = 0.15$ p.u.; (d) discrete-time design at $\omega_m = 2$ p.u. and $i_d = i_q = 0.15$ p.u. In all the cases, the sampling frequency is 2 kHz. The filled blue area defines the stability region for accurate parameter estimates. The dashed lines define the stability boundaries for $\hat{R}_s = 0.7R_s$ in (a, b) and for $\hat{L}_q = 0.7L_q$ in (c, d). The parameter selection (36) is shown by the dotted line and the red circles mark its value at the considered operating-point speed.

current to the flux. The controller gains have been scaled accordingly, so that the closed-loop dynamics remain the same. The flux-controller bandwidth is $2\pi \cdot 200$ rad/s. It is worth noticing that the performance and the stability of the control system would be significantly deteriorated, if the flux (or current) controller were designed in the continuous-time domain and then discretized, e.g., by using the forward Euler approximation. The control system shown in Fig. 2 is augmented with a PI-type speed controller, whose feedback signal is the speed estimate $\hat{\omega}_{mi}$ obtained from the observer.

Fig. 5 shows the flux-reference calculation scheme applied in this paper. A similar scheme for calculation of the current references has been proposed in [30]. One-dimensional look-up tables for the maximum-torque-per-ampere (MTPA) and maximum-torque-per-volt (MTPV) conditions as well as a two-dimensional look-up table $\psi_q = f(\psi_s, T_e)$ were calculated off-line using the same magnetic model [29], which is used in the observer. The fictitious flux ψ'_f should always be nonzero in sensorless back-EMF-based control methods. A minimum value for the stator flux is needed in the case of SyRMs, since very low values of ψ'_f also tend to decrease the robustness of back-EMF based methods. Here, the minimum value of the d-axis flux reference is $\psi_{d,ref} = 0.35$ Vs. The maximum value of the reference torque is limited to 150% of the rated torque. It is to be noted that the proposed observer design could be used also with different flux-reference (or current-reference) calculation methods.

The discrete-time flux observer (20)–(22) has been implemented using the proposed gains (30) and (34). The design parameters are selected in a similar manner as in [16],

$$b_c = b_{c0} + 0.75|\hat{\omega}_m|, \quad c_c = 1.5b_c|\hat{\omega}_m| \tag{36}$$

where $b_{c0} = 2\pi \cdot 20$ rad/s. The coefficient c_c is selected to keep the undamped natural frequency of the closed-loop flux-observer poles in the vicinity of the undamped natural frequency of the open-loop system poles. However, the damping of the open-loop system poles is poor at higher speeds. Thus, the coefficient b_c is selected to increase the damping of the closed-loop flux-observer poles in this region.

The poles of the speed-adaptation loop are placed according to the characteristic equation $s^2 + 2\zeta\omega_n s + \omega_n^2$, where ζ is the damping ratio and ω_n is the undamped natural frequency. In order to have fast speed-adaptation dynamics, ω_n should have a sufficiently high value. However, selecting too high value for ω_n may deteriorate the robustness of the speed-adaptation loop against noise and parameter errors. In this paper, $\omega_n = 2\pi \cdot 100$ rad/s and $\zeta = 1$ are selected, i.e., $d_c = 2\omega_n$ and $e_c = \omega_n^2$. The continuous-time design parameters are then mapped to their discrete-time equivalents by using (35).

V. Results

The sensorless control method with the proposed discrete-time observer design is evaluated by means of the stability analysis, simulations, and experiments. The stability analysis and simulation results corresponding to the continuous-time design with the forward Euler discretization are also presented for comparison.

A. Stability Analysis

The local stability of the nonlinear estimation-error dynamics is analyzed via linearized model shown in Fig. 4. Nonzero $\boldsymbol{b}_\omega$ in (27) is included in this numerical analysis, unlike in the analytical gain design in Section III-E. A state-space

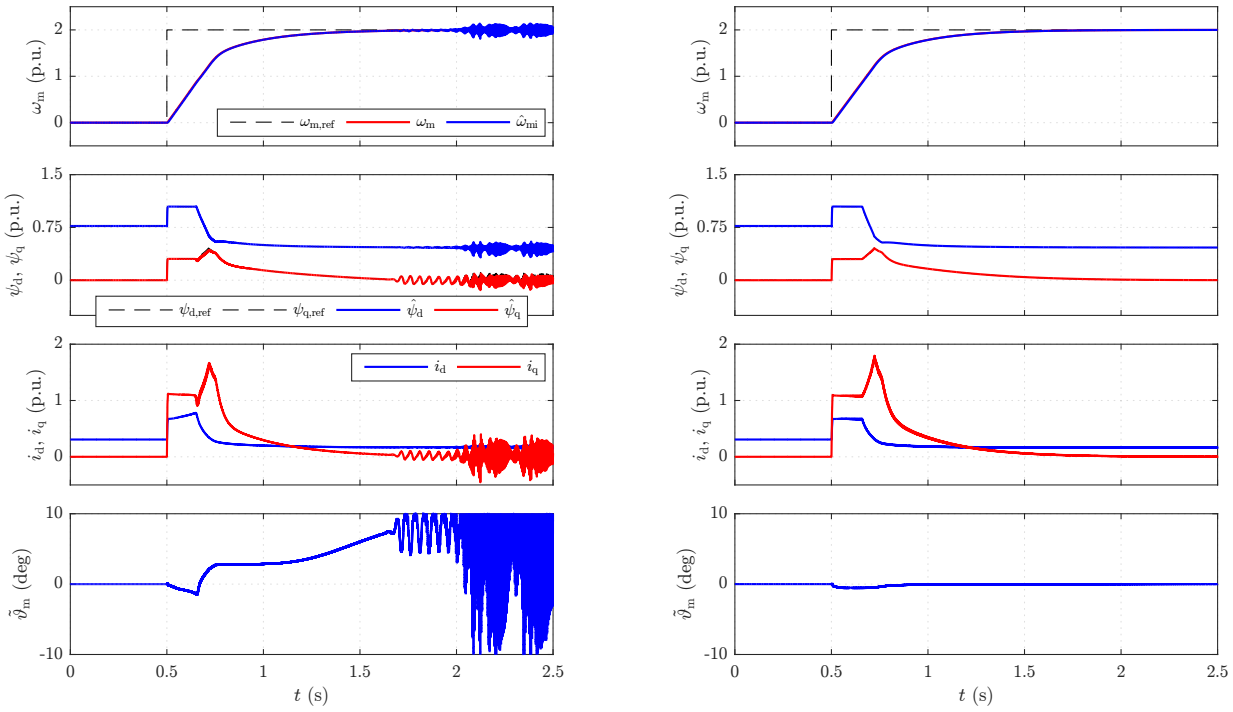

Fig. 7. Simulation results of a speed-reference step from 0 to 2 p.u. ($2\pi \cdot 211.6$ rad/s): (a) continuous-time observer design, discretized using the forward Euler approximation at the sampling frequency of 6 kHz; (b) discrete-time design at the sampling frequency of 2 kHz. The first subplot shows the reference speed $\omega_{\mathrm{m,ref}}$, actual speed ω_m, and estimated speed $\hat{\omega}_\mathrm{mi}$. The second subplot shows the reference and estimated flux components in estimated rotor coordinates (overlapping). The third subplot shows the measured current components, also in estimated rotor coordinates. The last subplot shows the estimation error $\tilde{\vartheta}_\mathrm{m} = \hat{\vartheta}_\mathrm{m} - \vartheta_\mathrm{m}$ of the rotor position (in electrical degrees).

representation corresponding to Fig. 4 is given in Appendix B, including the effects of the parameter errors. The linearized system is stable, if all the eigenvalues of the closed-loop system matrix [cf. $\boldsymbol{A}_\mathrm{cl}$ in (42) in Appendix B] are inside the unit circle. Otherwise, the linearized system is unstable. The sampling frequency is 2 kHz, i.e., the sampling period is $T_\mathrm{s} = 500$ μs. The actual parameters are: $R_\mathrm{s} = 0.54$ Ω, $L_\mathrm{d} = 41.5$ mH, and $L_\mathrm{q} = 6.2$ mH. Parameter estimates are marked with the hat. To simplify notation, the subscript 0 is dropped from the operating-point quantities in the following.

Fig. 6 illustrates the stability regions in the design parameter space at the speeds of 0.1 p.u. and 2 p.u. The design parameter c_c is scaled by the operating-point rotor speed, enabling the same axis scaling to be used in all the figures. Furthermore, the design parameter selection (36), which is used in the simulations and experiments, becomes a straight line in these coordinates. The values of (36) at the given speeds are marked by the red circles in the figures. Without discretization and parameter errors, the whole quadrant (where $b_\mathrm{c} > 0$ and $c_\mathrm{c} > 0$) would be stable.

First, the stability at the speed of 0.1 p.u. is considered in Figs. 6(a) and (b). The operating-point current components are $i_\mathrm{d} = 0.55$ p.u. and $i_\mathrm{q} = 0.90$ p.u., which correspond to 125% of the rated torque. The filled blue area defines the stability region in the design parameter space for accurate parameter estimates. Fig. 6(a) shows the results for the continuous-time design with the forward Euler approximation and Fig. 6(b) for the direct discrete-time design. It can be seen that the stability region of the discrete-time design is slightly larger than that of the continuous-time design. The dashed lines define the stability boundaries for $\hat{R}_\mathrm{s} = 0.7R_\mathrm{s}$; it can be seen that the stability regions in Figs. 6(a) and (b) are practically identical in this case. The parameter selection (36) is stable in the case of both the continuous-time and discrete-time designs.

Next, the speed of 2 p.u. is considered in Figs. 6(c) and (d). The operating-point current components are $i_\mathrm{d} = i_\mathrm{q} = 0.15$ p.u. Fig. 6(c) shows the results for the continuous-time design with the forward Euler discretization. It can be seen that there are no stable design parameter combinations if $b_\mathrm{c} < 2\pi \cdot 260$ rad/s, rendering the selection (36) unstable. Choosing a too large value for b_c would make the system highly sensitive to the noise. In the case of the discrete-time design shown in Fig. 6(d), almost the entire quadrant is stable, giving much freedom in the gain selection. The small unstable region near $b_\mathrm{c} = 0$ originates from nonzero $\boldsymbol{b}_\omega$, which was omitted in the gain selection. The areas bounded by the dashed lines show the stability regions for $\hat{L}_\mathrm{q} = 0.7L_\mathrm{q}$. For the discrete-time design, the parameter selection (36) is located clearly in the stable region, despite the parameter error.

B. Simulations

The focus on the following simulation and experimental results will be in the operation at higher speeds, where the differences between the two design approaches become prominent. The magnetic saturation in the motor model and the controller is modelled using the model in [29].

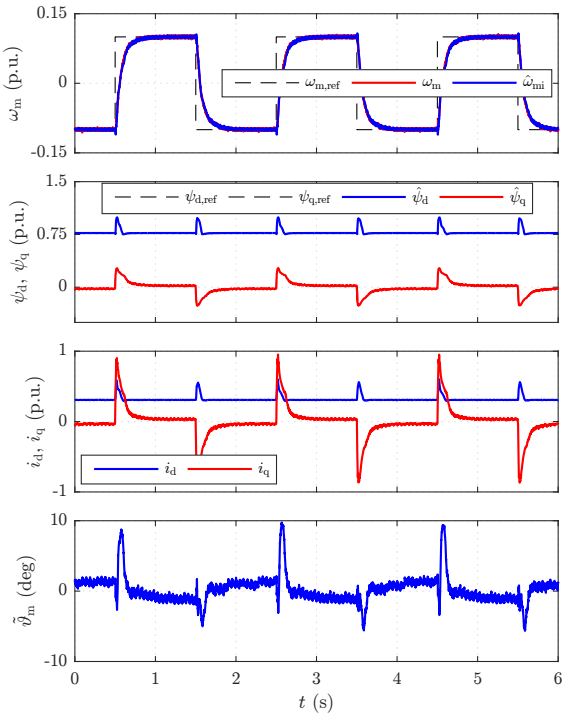

Fig. 8. Experimental results for the discrete-time design: speed reversals at low speeds. The sampling frequency is 2 kHz.

First, the continuous-time observer design, discretized using the forward Euler approximation, is considered. An example of simulation results at the sampling frequency of 6 kHz is shown in Fig. 7(a). The motor is accelerated from zero to the speed of 2 p.u. ($2\pi \cdot 211.6$ rad/s), resulting in the ratio of almost 30 between the sampling and fundamental frequencies. It can be seen that the system becomes unstable after $t = 1.6$ s. Further, it can be noticed that the error $\tilde{\vartheta}_\mathrm{m} = \hat{\vartheta}_\mathrm{m} - \vartheta_\mathrm{m}$ in the rotor position estimate increases with the rotor speed.

Fig. 7(b) shows the results for the proposed direct discrete-time design at the sampling frequency of 2 kHz. In this case, the ratio between the sampling and fundamental frequencies is below 10. It can be seen that the speed estimate follows the actual speed very well. The position estimation error is small during transient and converges quickly to zero. With the discrete-time design, the sampling frequency could still be lowered, even much below 1 kHz in the ideal case.

C. Experiments

The proposed discrete-time observer design is experimentally evaluated at the sampling frequency of 2 kHz. Before starting the motor, a constant current vector was fed to the direction of the a-phase magnetic axis—causing the rotor to rotate into this direction—and the rotor position estimate $\hat{\vartheta}_\mathrm{m}$ was reset to zero. Alternatively, the initial rotor position could be found using signal injection, without causing the rotor to move.

In the following, the rotor speed and position are estimated solely using the proposed observer and no additional starting algorithms are used. In theory, the estimation-error dynamics are only marginally stable at zero speed. In practice, the drive system remains stable and starting the motor is possible (with both the continuous and discrete-time designs), but the system does not tolerate the load torque at zero speed. If the motor parameter estimates are poorly known or the inverter nonlinearities are not compensated for, it is necessary to apply some low-speed starting algorithm, e.g., [31], or a signal-injection method. It is also to be noted that the speed estimate $\hat{\omega}_\mathrm{mi}$ comes directly from (22) without any low-pass filtering.

Fig. 8 shows example results at low speeds: the speed reference is stepped between -0.1 p.u. and 0.1 p.u. It can be seen that the speed estimate follows closely the actual measured speed. Generally, the low-speed performance of the discrete-time design is quite similar to the corresponding continuous-time design, cf. the results in [16] without signal injection and the results in [18] with signal injection. Fig. 9 shows an acceleration to the rated speed, a speed reversal, and a load torque step. It can be seen that the estimated speed $\hat{\omega}_\mathrm{mi}$ follows the actual speed very well and the estimation error $\tilde{\vartheta}_\mathrm{m}$ is also small (less than 5 electrical degrees in the steady state).

Fig. 10 shows the experimental results at high speeds, corresponding to the simulation case shown in Fig. 7(b). The motor is accelerated from zero to the speed of 2 p.u., resulting in the ratio below 10 between the sampling and fundamental frequencies. It can be seen that the estimated quantities are very smooth and the estimation error of the rotor position is small (about 6 electrical degrees in the steady state). Compared to the simulation results, there is more noise in the current waveforms. This noise consists mainly of low-order (sixth and lower orders) harmonics, which result from highly nonlinear saturation characteristics and spatial inductance harmonics of the prototype SyRM. However, despite these harmonics, the observer and control system works well.

VI. Conclusions

A speed-adaptive full-order observer for motion-sensorless IPM and SyRM drives was designed directly in the discrete-time domain. The hold-equivalent model applied in the design can be either the exact model or a series expansion. The design takes the effects of the ZOH and time delays inherently into account. The closed-loop estimation-error dynamics were linearized and the stabilizing gains were derived using the small-signal model. The stability of the proposed discrete-time design was compared with the continuous-time design using eigenvalue analysis and simulations. The performance of the proposed design was also evaluated using experiments on a 6.7-kW SyRM drive. Based on the results, performance improvements obtained via the direct discrete-time design—compared to the corresponding continuous-time designs—are significant, if the ratio between the sampling frequency and the fundamental frequency is low. For low-frequency operation, the system can be augmented with a signal-injection method.

Appendix A
Exact Discrete-Time Model

In the derivation of the model [25], the rotor speed and the motor parameters have been assumed to be constant during the

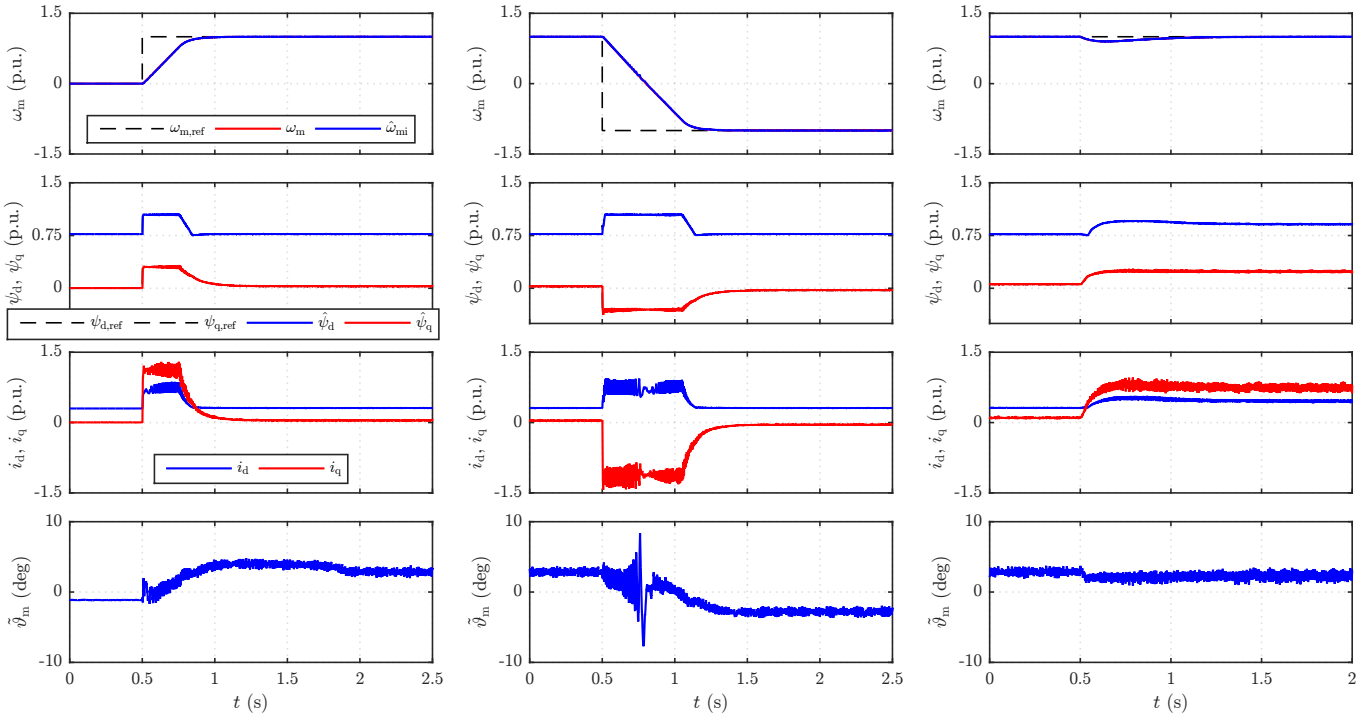

Fig. 9. Experimental results for the discrete-time design: (a) speed-reference step from 0 to 1 p.u.; (b) speed reversal; (c) load torque step. The sampling frequency is 2 kHz.

sampling period. The closed-form solutions for the elements of $\boldsymbol{\Phi}$ in (19) are

$$\begin{aligned}\phi_{11} &= \mathrm{e}^{-\sigma T_\mathrm{s}}\left[\cosh(\lambda T_\mathrm{s}) - \delta\frac{\sinh(\lambda T_\mathrm{s})}{\lambda}\right]\\ \phi_{22} &= \mathrm{e}^{-\sigma T_\mathrm{s}}\left[\cosh(\lambda T_\mathrm{s}) + \delta\frac{\sinh(\lambda T_\mathrm{s})}{\lambda}\right]\\ \phi_{21} &= -\omega_\mathrm{m}\mathrm{e}^{-\sigma T_\mathrm{s}}\frac{\sinh(\lambda T_\mathrm{s})}{\lambda}\end{aligned} \tag{37}$$

where $\lambda = \sqrt{\delta^2 - \omega_\mathrm{m}^2}$ and[2]

$$\sigma = \frac{R_\mathrm{s}}{2}\left(\frac{1}{L_\mathrm{d}} + \frac{1}{L_\mathrm{q}}\right), \quad \delta = \frac{R_\mathrm{s}}{2}\left(\frac{1}{L_\mathrm{d}} - \frac{1}{L_\mathrm{q}}\right). \tag{38}$$

The closed-form solutions for the elements of $\boldsymbol{\Gamma}$ in (19) are

$$\begin{aligned}\gamma_{11} &= G\Big[g_{11}\cos(\omega_\mathrm{m}T_\mathrm{s}) - g_{12}\sin(\omega_\mathrm{m}T_\mathrm{s}) - g_{11}\phi_{11}\\ &\qquad + (\sigma+\delta)\omega_\mathrm{m}^2(\phi_{11}-\phi_{22})\Big]\\ \gamma_{12} &= G\Big[g_{12}\cos(\omega_\mathrm{m}T_\mathrm{s}) + g_{11}\sin(\omega_\mathrm{m}T_\mathrm{s}) - g_{12}\phi_{11} + g_{22}\phi_{21}\Big]\\ \gamma_{21} &= G\Big[g_{21}\cos(\omega_\mathrm{m}T_\mathrm{s}) - g_{22}\sin(\omega_\mathrm{m}T_\mathrm{s}) - g_{21}\phi_{22} - g_{11}\phi_{21}\Big]\\ \gamma_{22} &= G\Big[g_{22}\cos(\omega_\mathrm{m}T_\mathrm{s}) + g_{21}\sin(\omega_\mathrm{m}T_\mathrm{s}) - g_{22}\phi_{22}\\ &\qquad + (\sigma-\delta)\omega_\mathrm{m}^2(\phi_{22}-\phi_{11})\Big]\end{aligned} \tag{39}$$

[2]If $\omega_\mathrm{m}^2 > \delta^2$, then $\lambda = \mathrm{j}\lambda_\mathrm{im} = \mathrm{j}\sqrt{\omega_\mathrm{m}^2 - \delta^2}$ is imaginary. All the matrix elements remain real since $\cosh(\mathrm{j}\lambda_\mathrm{im}T_\mathrm{s}) = \cos(\lambda_\mathrm{im}T_\mathrm{s})$ and $\sinh(\mathrm{j}\lambda_\mathrm{im}T_\mathrm{s})/(\mathrm{j}\lambda_\mathrm{im}) = \sin(\lambda_\mathrm{im}T_\mathrm{s})/\lambda_\mathrm{im}$ hold due to the properties of hyperbolic functions. Furthermore, for $\lambda = 0$, these functions reduce to $\cosh(\lambda T_\mathrm{s}) = \sinh(\lambda T_\mathrm{s})/\lambda = 1$.

where $G = 1/[(\sigma^2-\delta^2)^2 + 4\sigma^2\omega_\mathrm{m}^2]$ and

$$\begin{aligned}g_{11} &= (\sigma-\delta)^2(\sigma+\delta) + 4\sigma\omega_\mathrm{m}^2, \quad g_{12} = 2(\sigma-\delta)\delta\omega_\mathrm{m}\\ g_{21} &= 2(\sigma+\delta)\delta\omega_\mathrm{m}, \quad g_{22} = (\sigma+\delta)^2(\sigma-\delta) + 4\sigma\omega_\mathrm{m}^2.\end{aligned} \tag{40}$$

In the previous derivations, it is important to notice that $\mathrm{e}^{x+y} = \mathrm{e}^x\mathrm{e}^y$ does not hold for matrix exponentials in general. The elements of $\boldsymbol{\gamma}$ in (19) are given by

$$\begin{aligned}\gamma_1 &= H\left[(\sigma-\delta)(1-\phi_{11}) - \omega_\mathrm{m}\phi_{21}\right]\\ \gamma_2 &= H\left[-\sigma\phi_{21} + \omega_\mathrm{m}\left(\frac{\phi_{11}+\phi_{22}}{2} - 1\right)\right]\end{aligned} \tag{41}$$

where $H = (\sigma+\delta)/[(\sigma+\delta)(\sigma-\delta) + \omega_\mathrm{m}^2]$.

Appendix B
Dynamics With Erroneous System Matrices

With modeling errors included, the state-space representation of the linearized (autonomous) closed-loop system consisting of (20)–(23) is

$$\begin{bmatrix}\tilde{\boldsymbol{\psi}}_\mathrm{s}(k+1)\\ \tilde{\vartheta}_\mathrm{m}(k+1)\\ \tilde{\omega}_\mathrm{mi}(k+1)\end{bmatrix} = \underbrace{\begin{bmatrix}\boldsymbol{A}_\psi + \boldsymbol{b}_\omega\boldsymbol{k}_\mathrm{p}\hat{\boldsymbol{C}} & \boldsymbol{b}_\vartheta + \boldsymbol{b}_\omega\boldsymbol{k}_\mathrm{p}\boldsymbol{d}_\vartheta & \boldsymbol{b}_\omega\\ T_\mathrm{s}\boldsymbol{k}_\mathrm{p}\hat{\boldsymbol{C}} & 1 + T_\mathrm{s}\boldsymbol{k}_\mathrm{p}\boldsymbol{d}_\vartheta & T_\mathrm{s}\\ T_\mathrm{s}\boldsymbol{k}_\mathrm{i}\hat{\boldsymbol{C}} & T_\mathrm{s}\boldsymbol{k}_\mathrm{i}\boldsymbol{d}_\vartheta & 1\end{bmatrix}}_{\boldsymbol{A}_\mathrm{cl}}\begin{bmatrix}\tilde{\boldsymbol{\psi}}_\mathrm{s}(k)\\ \tilde{\vartheta}_\mathrm{m}(k)\\ \tilde{\omega}_\mathrm{mi}(k)\end{bmatrix} \tag{42}$$

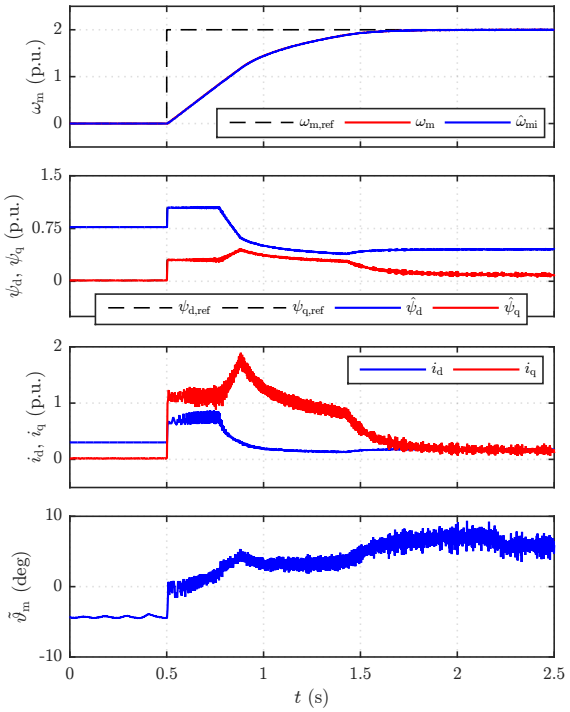

Fig. 10. Experimental results for the discrete-time design: speed reference is stepped from zero to the speed of 2 p.u. ($2\pi \cdot 211.6$ rad/s). The sampling frequency is 2 kHz.

where $\hat{\boldsymbol{C}}$ is the inverse of the inductance matrix estimate and the system matrices are

$$\boldsymbol{A}_\psi = \hat{\boldsymbol{\Phi}}_0 + \boldsymbol{K}\hat{\boldsymbol{C}}$$

$$\boldsymbol{b}_\omega = \left(\frac{\partial\hat{\boldsymbol{\Phi}}}{\partial\hat{\omega}_\mathrm{m}}\bigg|_0 + T_\mathrm{s}\mathbf{J}\boldsymbol{\Phi}_0\right)\boldsymbol{\psi}_{\mathrm{s}0} + \left(\frac{\partial\hat{\boldsymbol{\gamma}}}{\partial\hat{\omega}_\mathrm{m}}\bigg|_0 + T_\mathrm{s}\mathbf{J}\boldsymbol{\gamma}_0\right)\psi_\mathrm{f} + \left(\frac{\partial\hat{\boldsymbol{\Gamma}}}{\partial\hat{\omega}_\mathrm{m}}\bigg|_0 + T_\mathrm{s}\mathbf{J}\boldsymbol{\Gamma}_0\right)\boldsymbol{u}_{\mathrm{s}0} + \frac{\partial\hat{\boldsymbol{\gamma}}}{\partial\hat{\omega}_\mathrm{m}}\bigg|_0\tilde{\psi}_\mathrm{f} + \frac{\partial\hat{\boldsymbol{\Phi}}_0}{\partial\hat{\omega}_\mathrm{m}}\bigg|_0\tilde{\boldsymbol{\psi}}_{\mathrm{s}0}$$

$$\boldsymbol{b}_\vartheta = (\mathbf{J}\boldsymbol{\Phi}_0 - \boldsymbol{\Phi}_0\mathbf{J})\boldsymbol{\psi}_{\mathrm{s}0} + \mathbf{J}\boldsymbol{\gamma}_0\psi_\mathrm{f} + (\tilde{\boldsymbol{\Phi}}\hat{\boldsymbol{C}}^{-1} + \boldsymbol{K})\boldsymbol{d}_\vartheta + (\mathbf{J}\boldsymbol{\Gamma}_0 - \boldsymbol{\Gamma}_0\mathbf{J})\,\boldsymbol{u}_{\mathrm{s}0}$$

$$\boldsymbol{d}_\vartheta = \left(\hat{\boldsymbol{C}}\boldsymbol{C}^{-1}\mathbf{J}\boldsymbol{C} - \hat{\boldsymbol{C}}\mathbf{J}\right)\boldsymbol{\psi}_{\mathrm{s}0} + \hat{\boldsymbol{C}}\boldsymbol{C}^{-1}\mathbf{J}\boldsymbol{d}\psi_\mathrm{f}. \qquad (43)$$

The stability of the closed-loop system is determined by the eigenvalues of $\boldsymbol{A}_\mathrm{cl}$ in (42). Discretization errors and parameter errors affect the stability via erroneous $\hat{\boldsymbol{\Phi}}$, $\hat{\boldsymbol{\Gamma}}$, $\hat{\boldsymbol{\gamma}}$, $\hat{\boldsymbol{C}}$, and their derivatives with respect to the estimated speed.

The steady-state estimation errors in the operating point are generally nonzero, if there are discretization errors or parameter errors in the system. In order to be able to calculate the elements of the matrix $\boldsymbol{A}_\mathrm{cl}$, the operating point has to be first solved. It can be solved numerically from the following equations: (22) by setting $\hat{\omega}_\mathrm{mi}(k+1) = \hat{\omega}_\mathrm{mi}(k)$; (23) by setting $\boldsymbol{\psi}_\mathrm{s}(k+1) = \boldsymbol{\psi}_\mathrm{s}(k)$; and (25) by setting $\tilde{\boldsymbol{\psi}}_\mathrm{s}(k+1) = \tilde{\boldsymbol{\psi}}_\mathrm{s}(k)$, with the parameter errors included.

Acknowledgment

The authors would like to thank E. Mölsä for help in building the experimental setup and W. Khan for help in calculating look-up tables for the flux-reference calculation.

References

[1] G. Pellegrino, A. Vagati, P. Guglielmi, and B. Boazzo, "Performance comparison between surface-mounted and interior PM motor drives for electric vehicle application," *IEEE Trans. Ind. Electron.*, vol. 59, no. 2, pp. 803–811, Feb. 2012.

[2] J.-I. Ha, S.-J. Kang, and S.-K. Sul, "Position-controlled synchronous reluctance motor without rotational transducer," *IEEE Trans. Ind. Appl.*, vol. 35, no. 6, pp. 1393–1398, Nov./Dec. 1999.

[3] E. Capecchi, P. Guglielmo, M. Pastorelli, and A. Vagati, "Position-sensorless control of the transverse-laminated synchronous reluctance motor," *IEEE Trans. Ind. Appl.*, vol. 37, no. 6, pp. 1768–1776, Nov./Dec. 2001.

[4] H. F. Hofmann, S. R. Sanders, and A. EL-Antably, "Stator-flux-oriented vector control of synchronous reluctance machines with maximized efficiency," *IEEE Trans. Ind. Electron.*, vol. 51, no. 5, pp. 1066–1072, Oct. 2004.

[5] S. Koonlaboon and S. Sangwongwanich, "Sensorless control of interior permanent-magnet synchronous motors based on a fictitious permanent-magnet flux model," in *Conf. Rec. IEEE-IAS Annu. Meeting*, Hong Kong, Oct. 2005, pp. 1111–1118.

[6] O. Wallmark, L. Harnefors, and O. Carlson, "An improved speed and position estimator for salient permanent-magnet synchronous motors," *IEEE Trans. Ind. Electron.*, vol. 52, no. 1, pp. 255–262, Feb. 2005.

[7] A. Consoli, G. Scarcella, G. Scelba, A. Testa, and D. A. Triolo, "Sensorless rotor position estimation in synchronous reluctance motors exploiting a flux deviation approach," *IEEE Trans. Ind. Appl.*, vol. 43, no. 5, pp. 1266–1273, Sep./Oct. 2007.

[8] R. Morales-Caporal and M. Pacas, "Encoderless predictive direct torque control for synchronous reluctance machines at very low and zero speed," *IEEE Trans. Ind. Electron.*, vol. 55, no. 12, pp. 4408–4416, Dec. 2008.

[9] A. Piippo, M. Hinkkanen, and J. Luomi, "Analysis of an adaptive observer for sensorless control of interior permanent magnet synchronous motors," *IEEE Trans. Ind. Electron.*, vol. 55, no. 2, pp. 570–576, Feb. 2008.

[10] ——, "Adaptation of motor parameters in sensorless PMSM drives," *IEEE Trans. Ind. Appl.*, vol. 45, no. 1, pp. 203–212, Jan./Feb. 2009.

[11] W. Hammel and R. M. Kennel, "Position sensorless control of PMSM by synchronous injection and demodulation of alternating carrier voltage," in *Proc. IEEE SLED 2010*, Padova, Italy, July 2010, pp. 56–63.

[12] P. Landsmann, R. Kennel, H. de Kock, and M. Kamper, "Fundamental saliency based encoderless control for reluctance synchronous machines," in *Proc. ICEM'10*, Rome, Italy, Sept. 2010.

[13] A. Ghaderi and T. Hanamoto, "Wide-speed-range sensorless vector control of synchronous reluctance motors based on extended programmable cascaded low-pass filters," *IEEE Trans. Ind. Electron.*, vol. 58, no. 6, pp. 2322–2333, June 2011.

[14] K. Kato, M. Tomita, M. Hasegawa, S. Doki, S. Okuma, and S. Kato, "Position and velocity sensorless control of synchronous reluctance motor at low speed using disturbance observer for high-frequency extended EMF," in *Proc. IEEE IECON'11*, vol. 1, Melbourne, Australia, Nov. 2011, pp. 1971–1976.

[15] S.-C. Agarlită, I. Boldea, and F. Blaabjerg, "High-frequency-injection-assisted "active flux"-based sensorless vector control of reluctance synchronous motors, with experiments from zero speed," *IEEE Trans. Ind. Appl.*, vol. 48, no. 6, pp. 1931–1939, Nov./Dec. 2012.

[16] T. Tuovinen, M. Hinkkanen, L. Harnefors, and J. Luomi, "Comparison of a reduced-order observer and a full-order observer for sensorless synchronous motor drives," *IEEE Trans. Ind. Appl.*, vol. 48, no. 6, pp. 1959–1967, Nov./Dec. 2012.

[17] M.-Y. Wei and T.-H. Liu, "Design and implementation of an online tuning adaptive controller for synchronous reluctance motor drives," *IEEE Trans. Ind. Electron.*, vol. 60, no. 9, pp. 3644–3657, Sep. 2013.

[18] T. Tuovinen and M. Hinkkanen, "Adaptive full-order observer with high-frequency signal injection for synchronous reluctance motor drives," *IEEE J. Emerg. Sel. Topics Power Electron.*, vol. 2, no. 2, pp. 181–189, June 2014.

[19] W. Xu and R. D. Lorenz, "High-frequency injection-based stator flux linkage and torque estimation for DB-DTFC implementation on IPMSMs considering cross-saturation effects," *IEEE Trans. Ind. Appl.*, vol. 50, no. 6, pp. 3805–3815, Nov. 2014.

[20] K.-K. Huh and R. D. Lorenz, "Discrete-time domain modeling and design for AC machine current regulation," in *Conf. Rec. IEEE-IAS Annu. Meeting*, New Orleans, LA, Sept. 2007, pp. 2066–2073.

[21] H. Kim, M. W. Degner, J. M. Guerrero, F. Briz, and R. D. Lorenz, "Discrete-time current regulator design for AC machine drives," *IEEE Trans. Ind. Appl.*, vol. 46, no. 4, pp. 1425–1435, July/Aug. 2010.
[22] W. Peters, T. Huber, and J. Böcker, "Control realization for an interior permanent magnet synchronous motor (IPMSM) in automotive drive trains," in *Conf. PCIM 2011*, vol. 1, Nuremberg, Germany, May 2011, pp. 98–103.
[23] W. Peters and J. Böcker, "Discrete-time design of adaptive current controller for interior permanent magnet synchronous motors (IPMSM) with high magnetic saturation," in *Proc. IEEE IECON'13*, Vienna, Austria, Nov. 2013, pp. 6608–6613.
[24] J. S. Lee, C.-H. Choi, J.-K. Seok, and R. D. Lorenz, "Deadbeat-direct torque and flux control of interior permanent magnet synchronous machines with discrete time stator current and stator flux linkage observer," *IEEE Trans. Ind. Appl.*, vol. 47, no. 4, pp. 1749–1758, July/Aug. 2011.
[25] M. Hinkkanen, H. A. A. Awan, Z. Qu, T. Tuovinen, and F. Briz, "Current control for synchronous motor drives: direct discrete-time pole-placement design," *IEEE Trans. Ind. Appl.*, vol. 52, no. 2, pp. 1530–1541, Mar./Apr. 2016.
[26] A. Vagati, M. Pastorelli, G. Fanceschini, and V. Drogoreanu, "Flux-observer-based high-performance control of synchronous reluctance motors by including cross saturation," *IEEE Trans. Ind. Appl.*, vol. 35, no. 3, pp. 597–605, May/June 1999.
[27] J. Böcker, S. Beineke, and A. Bähr, "On the control bandwidth of servo drives," in *Proc. EPE 2009*, Barcelona, Spain, Sept. 2009.
[28] N. Hoffmann, F. W. Fuchs, and J. Dannehl, "Models and effects of different updating and sampling concepts to the control of grid-connected PWM converters — a study based on discrete time domain analysis," in *Proc. EPE 2011*, Birmingham, UK, Aug./Sept. 2011.
[29] Z. Qu, T. Tuovinen, and M. Hinkkanen, "Inclusion of magnetic saturation in dynamic models of synchronous reluctance motors," in *Proc. ICEM'12*, Marseille, France, Sept. 2012, pp. 994–1000.
[30] M. Meyer and J. Böcker, "Optimum control for interior permanent magnet synchronous motors (IPMSM) in constant torque and flux weakening range," in *Proc. EPE-PEMC 2006*, Portoroz, Slovenia, Aug./Sept. 2006, pp. 282–286.
[31] S.-C. Agarlită, M. Fătu, L. N. Tutelea, F. Blaabjerg, and I. Boldea, "I-f starting and active flux based sensorless vector control of reluctance synchronous motors, with experiments," in *Proc. Optim'10*, vol. 1, Brasov, Romania, May 2010, pp. 337–342.

Hafiz Asad Ali Awan received the B.Sc. degree in electrical engineering from the University of Engineering and Technology, Lahore, Pakistan, in 2012 and the M.Sc.(Tech.) degree in electrical engineering from Aalto University, Espoo, Finland, in 2015.

He is currently working toward the D.Sc.(Tech.) degree at Aalto University. His main research interest is the control of electric drives.

Toni Tuovinen received the M.Sc. degree from the University of Helsinki, Helsinki, Finland, in 2005, the M.Sc.(Eng.) degree from Helsinki University of Technology, Espoo, Finland, in 2009, and the D.Sc.(Tech.) degree from Aalto University, Espoo, in 2014.

He is currently a Senior Design Engineer with ABB Oy Drives, Helsinki. His main research interests include the control of electric drives.

Seppo E. Saarakkala received the M.Sc.(Eng.) degree from Lappeenranta University of Technology, Lappeenranta, Finland, in 2008 and the D.Sc.(Tech.) degree from Aalto University, Espoo, Finland, in 2014.

Since 2010, he has been with the School of Electrical Engineering, Aalto University, where he is currently a Post-Doctoral Research Scientist. His main research interests include control systems and electric drives.

Marko Hinkkanen (M'06–SM'13) received the M.Sc.(Eng.) and D.Sc.(Tech.) degrees from Helsinki University of Technology, Espoo, Finland, in 2000 and 2004, respectively.

He is currently an Assistant Professor with the School of Electrical Engineering, Aalto University, Espoo. He has authored or co-authored more than 100 technical papers of which over 30 in IEEE journals. His research interests include control systems, electric drives, and power converters. Dr. Hinkkanen is an Editorial Board Member of the IET ELECTRIC POWER APPLICATIONS.